Optical properties and electronic structure of single crystals of $LuAl_2$ and $YbAl_2$

S. J. Lee, S. Y. Hong,* I. R. Fisher, P. C. Canfield, B. N. Harmon, and D. W. Lynch
Ames Laboratory and Department of Physics and Astronomy, Iowa State University, Ames, Iowa 50011
(Received 12 April 1999)

The optical conductivities of single crystals of $LuAl_2$ and $YbAl_2$ were measured by spectroscopic ellipsometry in the energy range of 1.4–5.5 eV for $LuAl_2$ and 1.4–5.2 eV for $YbAl_2$. The optical conductivity spectra of $LuAl_2$ and $YbAl_2$ show similar features except for a difference in magnitude. Both have peaks near 1.8–2.1 eV and broad shoulders between 3.0 and 4.0 eV. The shoulder is weaker in $YbAl_2$. The band structure, density of states, and optical conductivity were calculated with the tight-binding linear muffin-tin orbital method in the atomic sphere approximation. The calculated optical conductivity with the inclusion of energy-dependent broadening agrees well with the experimental data. Oxidation effects on the surface of the sample were modeled using a three-phase model. The calculated optical conductivity of the clean surface is enhanced over that of the oxidized surface.

I. INTRODUCTION

The rare-earth dialuminides, RAl_2 (R=rare earth), have been investigated extensively because they show a variety of physical phenomena and properties: magnetism,[1–4] superconductivity,[5,6] de Haas–van Alphen effect,[7] thermal property,[8] and electronic properties.[9–16] Nevertheless, the role of $4f$ electrons in determining the physical characteristics of these materials is still under investigation. Jarlborg *et al.*[16] calculated the energy band structure of $CeAl_2$, $LaAl_2$, and YAl_2 using the linear muffin-tin orbital (LMTO) method, neglecting spin-orbit coupling for the valence states. They found that the rare-earth atoms are the dominant factor in determining the electronic structure near the Fermi energy because the f bands are located close to the Fermi level. Kim and Lynch[17] measured the optical properties of polycrystalline $CeAl_2$ and $LuAl_2$ using rotating-polarizer-analyzer ellipsometry and reflectivity measurements in the 0.04–4.5 eV region at room temperature to study involvement of the $4f$ states in optical transitions. They found that the optical conductivity of $CeAl_2$ has structures at 0.1 eV and 1.0 eV while $LuAl_2$ has no structure below 1 eV. The difference in optical conductivities between $CeAl_2$ and $LuAl_2$ arises primarily from the different electronic structures involving the $4f$ states. In the case of $CeAl_2$, the $4f$ states are located near the Fermi level, while for $LuAl_2$ the $4f$ states are located well below the Fermi level. Therefore in the case of $CeAl_2$, the $4f$ states can contribute to interband transitions at lower energies, but for $LuAl_2$ interband contributions involving the $4f$ states occur only at higher energies (>5 eV).

The calculated[18] $4f$ bands for metallic elemental Yb are split by the spin-orbit interaction, and the locations of the fully occupied split bands are at 0.3 eV and 1.64 eV below the Fermi energy. X-ray photoemission (XPS) measurements on evaporated films of Yb showed that the spin-orbit split $4f$ levels are located at 1.4 ± 0.4 eV and 2.7 ± 0.4 eV below the Fermi level.[19] The difference in the energy position of the $4f$ levels between theory and experiment is about 1 eV. This is not surprising, since describing the final state spectrum with the one-electron approximation is not appropriate for an open-shell $4f$ system. The theoretical estimation of the $4f$-electron excitation energies, which can be measured by XPS and bremsstrahlung isochromat spectroscopy (BIS), has been performed by taking the total energy difference between the initial ground state and the final excited state obtained by self-consistent local-density approximation (LDA) calculations.[20]

In this paper we use the single-particle energies rather than the total energies to calculate the optical spectra. This may cause problems if $4f$ states are involved in the transitions. For the energy range considered this is not a problem for $LuAl_2$ since the $4f$ states are quite low in energy, but for $YbAl_2$ the $4f$ states near the Fermi level do influence the calculated low-energy optical conductivity. Experiments in the low-energy region are not yet available to test the adequacy of the single-particle approximation for the $YbAl_2$ spectra.

The crystal structure of $(Lu,Yb)Al_2$ is shown in Fig. 1. The rare-earth intermetallic compounds $LuAl_2$ and $YbAl_2$ crystallize in the cubic Laves $MgCu_2$ ($C15$) structure. The

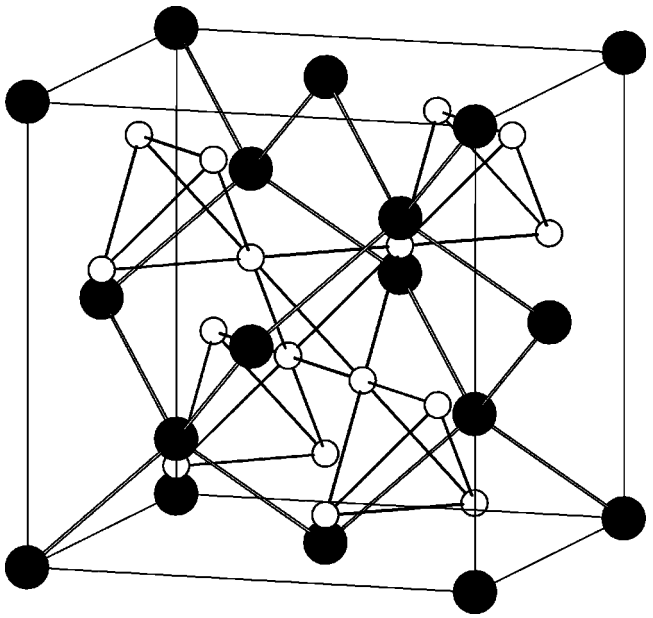

FIG. 1. Crystal structure of RAl_2 (R=Lu,Yb). The large black circles denote the sites of R atoms and the small open circles denote the sites of Al atoms.

rare-earth atoms are arranged in the diamond structure consisting of two fcc structures displaced from each other by one-fourth of a body diagonal. The Al atoms are arranged on sites of rhombohedral symmetry ($\bar{3}m$) in tetrahedra having four rare-earth atoms as the next-nearest neighbors. This $MgCu_2$ structure belongs to the space group O_h^7-$Fd3m$ with 24 atoms per conventional cubic unit cell (6 in the primitive unit cell).

In this paper we will present the real part of the diagonal conductivity, the density of states (DOS) and the band structures of $LuAl_2$ and $YbAl_2$ obtained by the tight-binding (TB) LMTO method. The agreement between the theoretical and experimental optical conductivity is good except for the magnitude differences between them. The differences in magnitude between theory and experiment may arise, in part, from oxidation effects on the sample surface. If there is no oxide on the surface of a sample, then the dielectric function or the optical conductivity can be obtained using a two-phase (air-sample) model. But since the sample is exposed to air during measurement, oxidation cannot be avoided. We considered the effect of oxidation through a three-phase (air–thin-oxide layer–clean-sample) model. The derived optical conductivity of the clean sample by the three-phase model shows enhancement of features from the measured spectrum.

II. SAMPLE PREPARATION AND CHARACTERIZATION

Single crystals have some advantages over polycrystalline samples or thin films in that they have a higher purity, perfect crystal periodicity, and good characterization, which is manifested in reproducibility of data with samples from different growths. One disadvantage of single crystals is frequently their small size, leading to difficulty in some experimental measurements such as ellipsometry. Single crystals of $YbAl_2$ and $LuAl_2$ were prepared via two different flux-growth techniques. For $YbAl_2$, elemental Yb and Al in the ratio of $Yb_{0.55}Al_{0.45}$ were placed in a sealed Ta crucible, which was placed in a sealed quartz tube, heated to 1190 °C, and slowly cooled to 750 °C, at which temperature the crystals were removed from the melt. These crystals were octahedral, with typical dimensions of $2\times2\times0.5$ mm^3. However, when applied to $LuAl_2$, this technique produces small, intergrown crystals. Hence, $LuAl_2$ was grown from a third element flux, in this case indium (In). The ternary melt was cooled slowly to 725 °C, at which temperature the crystals were removed from the flux. These crystals were larger than those produced from the binary melt and had both octahedral and platelike morphologies. In the case of the platelike samples, the growth direction is along [111]. The surfaces of the single crystals of $LuAl_2$ and $YbAl_2$ were somewhat dull due to the remnant flux on the surface of the crystal. We used only an alumina abrasive of 0.05 μm diameter to remove the remnant flux from the surface. After a short period of polishing, the surface became mirrorlike and did not require further treatment. X-ray powder diffraction patterns of $LuAl_2$ and $YbAl_2$ were measured at room temperature by crushing single crystals. From these, the lattice constants for $LuAl_2$ and $YbAl_2$ were determined as 7.746 Å and 7.885 Å , respectively. These are similar to those of previous literature data, which are 7.742 Å and 7.881 Å , respectively.[21,22] The lower limit for the detection of second phases in x-ray patterns is generally a few percent for both samples.

III. ELLIPSOMETRY

Ellipsometry is widely used to characterize surfaces, interfaces, and thin films. The principle of ellipsometry is based on the fact that the state of polarization of light is changed on reflection. This change is directly related to the dielectric function of the reflecting material. With rotating analyzer ellipsometry[23,24] (RAE) one measures the complex reflectivity ratio

$$\rho=\frac{r_p}{r_s}=\left|\frac{r_p}{r_s}\right|e^{i\Delta}=\tan\Psi e^{i\Delta}, \tag{1}$$

where r_p, r_s are the complex amplitude reflection coefficients for *p*- and *s*-polarized light and Ψ and Δ express the change in amplitude and phase between *p* and *s* components of polarized light reflected from a surface. Ψ and Δ are quantities directly measurable from ellipsometry.

IV. TWO-PHASE AND THREE-PHASE MODELS

The complex reflectivity ratio ρ given in Eq. (1) can be expressed with the angle of incidence ϕ_0 and complex dielectric function ϵ by[25]

$$\rho=\frac{\sin^2\phi_0-\cos\phi_0\sqrt{\epsilon-\sin^2\phi_0}}{\sin^2\phi_0+\cos\phi_0\sqrt{\epsilon-\sin^2\phi_0}}. \tag{2}$$

This is obtained using the two-phase model, that is, the system consists of an isotropic ambient and an isotropic semi-infinite, homogeneous solid. The interface between them is assumed to be abrupt and flat. The two media are related by Snell's law $n_0\sin\phi_0=n_1\sin\phi_1$, where n_0 and n_1 are the refractive indices for the ambient and homogeneous solid medium. The complex dielectric function ϵ is related to the complex refractive indices of the media by $\epsilon=\sqrt{n_1/n_0}$. One can easily show that the complex dielectric function ϵ is related to the complex reflectivity ratio ρ given in Eq. (2) by

$$\epsilon=\sin^2\phi_0+\sin^2\phi_0\tan^2\phi_0\left[\frac{1-\rho}{1+\rho}\right], \tag{3}$$

after simple derivation. Once we have the experimental data, ρ and ϕ_0, we can obtain a dielectric function.

In real situations, the two-phase model may not be appropriate. A native oxide layer on the surface requires the use a three-phase model to describe the real system and to derive the effective dielectric function of the oxidized sample. It is obtained from the dielectric functions of the clean bulk sample and its oxide. A good example of the three-phase model with a native oxide layer is the air-SiO_2-Si system, which has been studied by many authors.[26–28] Rossow[29] has calculated the effective dielectric function of GaAs using the dielectric functions of GaAs and its oxide. He found that the height of the imaginary part of the dielectric function of the oxidized sample, especially near the E_2 peak, is affected, that is, the magnitude of the peak at 4.7 eV is reduced greatly as the oxide thickness increases. Conversely, with the dielectric functions of an oxidized sample and its oxide layer, one can

obtain the dielectric function of the clean sample. The complex reflectance ratio for the three-phase model[25] is given by the following equation:

$$\rho = \frac{r_{01p} + r_{12p} e^{i2\beta}}{1 + r_{01p} r_{12p} e^{i2\beta}} \frac{1 + r_{01s} r_{12s} e^{i2\beta}}{r_{01s} + r_{12s} e^{i2\beta}}, \tag{4}$$

where the subscripts 0, 1, and 2 in the above equations represent the ambient, the layer, and bulk sample, and p and s stand for p and s polarization, respectively. The reflection coefficients for p and s polarized light between the i-j interface are given by

$$r_{ijp} = \frac{\epsilon_j \sqrt{\epsilon_i - \sin^2\phi_0} - \epsilon_i \sqrt{\epsilon_j - \sin^2\phi_0}}{\epsilon_j \sqrt{\epsilon_i - \sin^2\phi_0} + \epsilon_i \sqrt{\epsilon_j - \sin^2\phi_0}}, \tag{5}$$

$$r_{ijs} = \frac{\sqrt{\epsilon_i - \sin^2\phi_0} - \sqrt{\epsilon_j - \sin^2\phi_0}}{\sqrt{\epsilon_i - \sin^2\phi_0} + \sqrt{\epsilon_j - \sin^2\phi_0}}. \tag{6}$$

For example, r_{01p} is the reflection coefficient for p polarized light at the interface between ambient and the overlayer. The phase shift β is given by

$$\beta = \frac{2\pi d_{layer}}{\lambda} n_1 \cos\phi_1 = \frac{2\pi d_{layer}}{\lambda} \sqrt{n_1^2 - n_0^2 \sin^2\phi_0}, \tag{7}$$

where λ is the wavelength of the incident polarized light, ϕ_0 is the angle of incidence in ambient medium and ϕ_1 is the angle of refraction in the oxide layer n_1. By Snell's law, ϕ_0, ϕ_1, and ϕ_2, which are complex angles between the directions of propagation of the plane waves in the ambient (n_0), layer (n_1), bulk substrate (n_2) and the normal to the layer and the clean bulk sample, are related each other by

$$n_0 \sin\phi_0 = n_1 \sin\phi_1 = n_2 \sin\phi_2. \tag{8}$$

To describe the three-phase model system, we need six parameters. Three are the (in general, complex) refractive indices of the ambient (n_0), layer (n_1), and bulk substrate (n_2). These refractive indices will be real or complex depending on whether there is absorption. The other three are the thickness of the layer (d_{layer}), angle of incidence (ϕ_0), and wavelength of incident light (λ). In each measurement at one wavelength λ and one angle of incidence ϕ_0, we can determine only one complex unknown parameter or two real unknown parameters of the three-phase model system. For example, the complex refractive index of the pure bulk, n_2, can be determined only if the oxide overlayer thickness d_{layer} and refractive index n_1 are known. The two unknown optical parameters can be obtained by minimizing

$$M = |\rho^m - \rho^c(n_0, n_1, n_2, d_{layer}, \phi_0, \lambda)|^2, \tag{9}$$

where ρ^m is the ratio of the complex-amplitude reflection coefficients for p- and s-polarized light as defined in Eq. (1) for the ith measurement on a three-phase model system, ρ^c is the computed value of this ratio from Eq. (4).

For $LuAl_2$ we measured from 1.4 to 5.5 eV with an energy step of 0.02 eV. For $YbAl_2$ we measured from 1.4 to 5.2 eV with the same energy step. For this nonlinear least-squares fitting, the well-known Levenberg-Marquardt algorithm[30] has been employed. In Eq. (9), the refractive index n_0 of the ambient air is 1. The angle of incidence ϕ_0 and the wavelength λ are known parameters. Therefore there are three unknown parameters (two real and one complex), that is, the refractive index of the overlayer n_1, the thickness of the overlayer d_{layer}, and the complex refractive index of the clean bulk substrate n_2. To get the dielectric function of the clean bulk substrate, we need to know the refractive index n_1 and thickness d_{layer} of the oxide overlayer covering the bulk sample. There are many difficulties in obtaining accurate information on these. Therefore we assumed a constant value of the refractive index of the oxide layer and varied the thickness of the oxide layer, as will be discussed in detail later. With this information, the algorithm adjusts the unknown three-phase model parameters (complex refractive index of the clean bulk substrate) iteratively until the difference between the measured complex reflectance ratio and the complex reflectance ratio determined from three-phase model, Eq. (4), is minimized.

V. BAND-STRUCTURE CALCULATIONS

For the band-structure calculation, the tight-binding linear muffin-tin orbital (TB-LMTO) method based on the atomic-sphere approximation (ASA) with the inclusion of spin-orbit coupling is employed. The spin-orbit interaction lifts some of the degeneracies of the energy bands at high symmetry points or lines in k space. It couples the spin-up and spin-down states and doubles the size of the Hamiltonian matrix from that of the scalar-relativistic one-spin Hamiltonian matrix. It is well known that as the packing ratio of the crystal increases, the accuracy of the band-structure calculation improves for the TB-LMTO method. The structures of $LuAl_2$ and $YbAl_2$ are appropriate for the TB-LMTO method because they are closely packed structures with high symmetry. We used the room-temperature lattice constants for $LuAl_2$ and $YbAl_2$ obtained from the x-ray powder diffraction patterns.

We treated the $4f$ electrons of the rare-earth atoms as valence electrons throughout the whole calculation. The exchange-correlation potential has been included in the local-density approximation (LDA) with the von Barth–Hedin form.[31] The k-integrated functions have been evaluated by the tetrahedron technique with 144 k points in the irreducible Brillouin zone, which is $\frac{1}{48}$ of the Brillouin zone. Once the self-consistent potential and charge are obtained, the real part of the optical conductivity can be calculated. In cubic systems it is necessary to calculate only one of the three equal diagonal components of the conductivity tensor. We used Kubo's linear response theory,[32] which leads to interband contributions to the conductivity of the following form:

$$\sigma_{xx} = \frac{\pi e^2}{3m^2\omega} \sum_{f,i} \int_{BZ} d^3k \frac{2}{(2\pi)^2} |p_{fi}|^2 f_i(k)[1 - f_f(k)] \times \delta(E_f(k) - E_i(k) - \hbar\omega) \tag{10}$$

where BZ denotes the Brillouin zone, $f(k)$ is the Fermi distribution function, and i, f stand for the occupied initial and unoccupied final energy band states at wave vector k, respectively.

$$p_{fi}=\frac{\hbar}{i}\langle f|\nabla|i\rangle \tag{11}$$

is the dipole matrix element between the occupied $E_i(k)$ and unoccupied $E_f(k)$ one-electron states. The calculated spectra are unbroadened quantities. Improvement to this formalism comes from consideration of correlated interacting electrons as described by the quasiparticle picture. This picture describes changes in the single-particle picture using self-energy terms. The self-energy is usually momentum and energy dependent and consists of two parts,[33]

$$\Sigma=\Sigma_1+i\Sigma_2. \tag{12}$$

The real part of the self-energy represents a shift of the one-electron energy of a state, while the imaginary part describes the broadening of the energy level caused by the finite lifetime of a state. To consider the broadened experimental optical conductivity, the theoretical optical conductivity was convoluted with an energy-dependent Lorentzian broadening function[34] of width equal to the imaginary part of the complex self-energy, which was set empirically to $\Sigma_2(E)=0.1E$, where E is the incident photon energy. The real part of the self-energy was not considered in this calculation because the shift of the peak position of theoretical data from that of the experimental spectra is small (<0.2 eV). From the energy bands and the TB-LMTO eigenvectors, we calculated the total and orbital projected density of states.

VI. OXIDE EFFECTS

In experiments, the effects of oxidation, surface roughness, defects, and contamination are contained in the measured data. A measured dielectric function ϵ containing all these effects is called the effective dielectric function or pseudodielectric function, written as $\langle\epsilon\rangle$. The exact composition of a mixed oxide is difficult to determine. The rate of oxidation depends on several variables. Among them, high temperature and humidity increase the rate of oxidation. Light rare earths like Ce oxidize considerably faster than heavy rare-earth metals (Gd, Lu, Yb, etc.).[35] Zukowska[36] confirmed the formation of an Yb_2O_3 overlayer on an ytterbium surface by a structural examination after removing the ytterbium from the vacuum chamber. The real situation of the oxidized surface may be more complicated than is assumed with the Bruggemann effective-medium theory (BEMT) due to possible inhomogeneity of the oxide.[37]

Yb_2O_3 and Al_2O_3 are not only the possible oxides on $YbAl_2$. $YbAlO_3$ or other forms of ternary oxide are possible. $(YbAl)_2O_3$, a random mixture of Yb and Al oxides, is also possible. The oxide may be amorphous rather than crystalline. The dielectric functions for some of these possible oxide layers are not known. In order to estimate the optical constants of the clean bulk $YbAl_2$ by the three-phase model, we assumed a constant effective refractive index for the complicated oxide layer. The refractive indices[38] of Al_2O_3 and Yb_2O_3 are roughly 1.65 and 1.85 in the visible region. Therefore we take the assumed effective refractive index of the oxide layer of $YbAl_2$ as 1.7. It is well known that the oxide thickness of Al_2O_3 saturates below 30 Å when Al is exposed to air. Zukowska and Oleszkiewicz[39] estimated the thickness of the ytterbium oxide layer on the ytterbium substrate. They found that it slowly increases up to 22 Å within 24 hours of exposure to air, and the oxide layer stabilized at a value of 33 Å after 48 hours. Burnham and Jameson measured the oxidation rate of ytterbium in air by a simple optical transmission technique.[40] They measured the optical density of Yb thin films deposited on glass slides with a densitometer. From this method, they found the oxidation rate of Yb in air decreases quickly and estimated that the thickness of the oxide overlayer on Yb was about 90 Å after two months exposure to air, by extrapolation of their measurements. Because we did the ellipsometric measurements as soon as we finished a short period of polishing to remove the remnant flux from the surfaces, the thickness of the oxide probably does not exceed 50 Å. We varied the thickness of the unknown oxide layer from 20 Å to 50 Å in the three-phase model calculation.

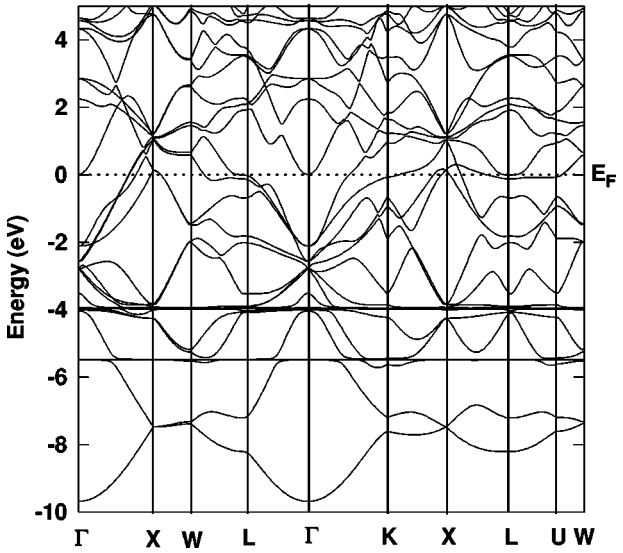

FIG. 2. Band structure of $LuAl_2$ obtained from the self-consistent TB LMTO with the spin-orbit interaction included.

VII. RESULTS AND DISCUSSION

The calculated electronic band structures of $LuAl_2$ and $YbAl_2$ are shown in Figs. 2 and 3. The Fermi energy E_F is marked by a horizontal dotted line and the symmetry points are indicated by vertical lines. In both calculations we treated the $4f$ electrons of Lu and Yb as valence electrons. Two narrow flat $4f$ bands, separated due to the spin-orbit interaction, lie 4.0 and 5.5 eV below the Fermi level for $LuAl_2$ and 0.2 and 1.8 eV below the Fermi level for $YbAl_2$, respectively. In the case of $YbAl_2$, a small fraction of the $4f_{7/2}$ bands extends to the Fermi level while the $4f$ electron bands are located well below the Fermi level for $LuAl_2$. The lowest two bands of $LuAl_2$ and $YbAl_2$, which are located between -10 and -6 eV, are mainly of Al s and p character. The theoretical partial densities of states for $LuAl_2$ and $YbAl_2$ obtained from TB-LMTO with LDA in the ASA are shown in Figs. 4 and 5, respectively. The calculated partial densities of states for $LuAl_2$ is similar to those of Takegahara.[41] He calculated the partial densities of states by a self-consistent augmented plane wave (APW) without the spin-orbit interaction, so there was no spin-orbit splitting in the $4f$ states.

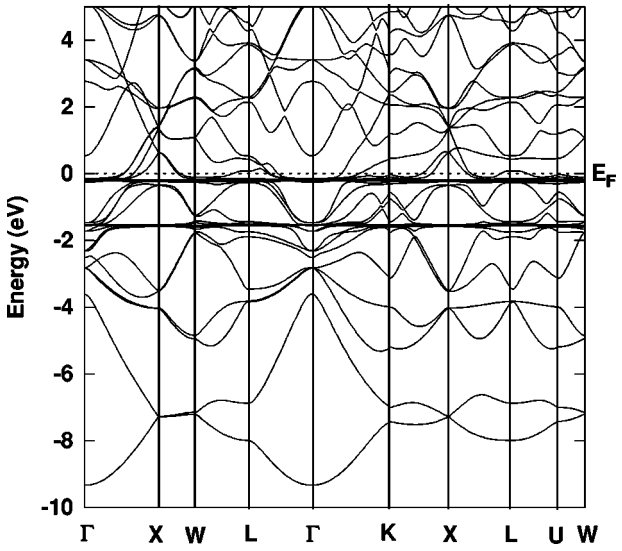

FIG. 3. Band structure of $YbAl_2$ obtained from the self-consistent TB LMTO with the spin-orbit interaction included.

There have been no reports on the theoretical electronic structure calculation for $YbAl_2$ as far as we know, so we could not compare our results with others. Due to the extended $4f_{7/2}$ state at the Fermi level in $YbAl_2$, the theoretical density of states of $YbAl_2$ at the Fermi level is nearly twice as large as that of $LuAl_2$ for which the $4f$ electron states are located well below the Fermi level.

The coefficient γ of electronic specific heat is given by

$$\gamma = \frac{\pi^2}{3} N(E_F) k_B^2 (1+\lambda), \tag{13}$$

where $N(E_F)$ is the density of states at the Fermi energy, k_B is Boltzmann's constant, and λ is the mass-enhancement factor. The experimental values of γ can be compared with the theoretical values obtained from the density of states at the Fermi energy. The experimental electronic specific heat coefficient γ of $YbAl_2$ has been reported to be $16.8\ \mathrm{mJ\,K^{-2}\,mol^{-1}}$ while that of $LuAl_2$ is $5.6\ \mathrm{mJ\,K^{-2}\,mol^{-1}}$.[42,43] The theoretical values are $7.81\ \mathrm{mJ\,K^{-2}\,mol^{-1}}$ and $4.08\ \mathrm{mJ\,K^{-2}\,mol^{-1}}$, respectively, with the TB-LMTO method. The difference between the calculated and measured γ is due to the mass-enhancement factor due to electron correlations incorporating the interactions of an electron with other electrons or phonons. Since γ is proportional to the density of states at the Fermi level, the larger γ of $YbAl_2$ than that of $LuAl_2$ implies a larger density of $YbAl_2$ at the Fermi level due to the presence of $4f$ states of $YbAl_2$ lying close to the Fermi level while those of $LuAl_2$ stay far below the Fermi level.

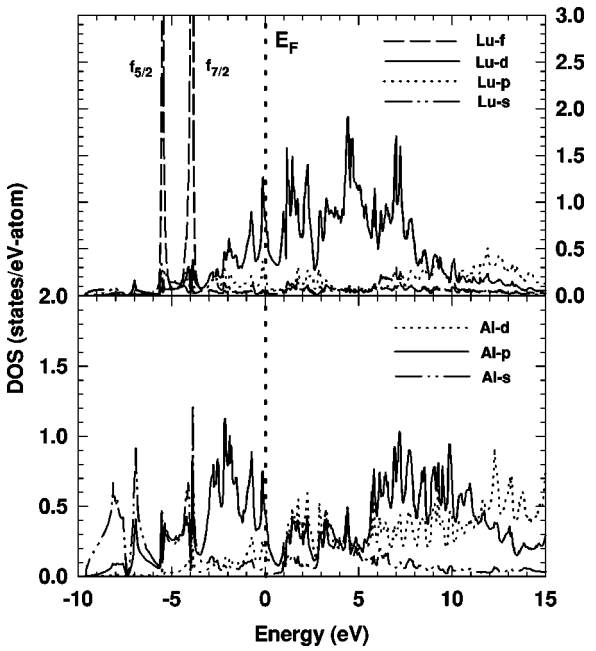

FIG. 4. Partial density of states obtained from the TB LMTO with the LDA in the ASA. The upper and lower panel show the DOS on the Lu and Al site in states/eV atom.

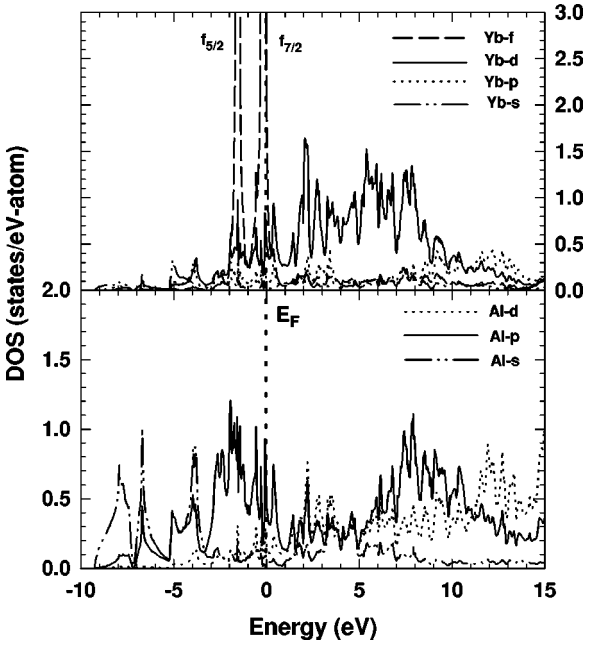

FIG. 5. Partial density of states obtained from the TB LMTO with the LDA in the ASA. The upper and lower panel show the DOS on the Yb and Al site in states/eV atom.

Bremsstrahlung isochromat spectroscopy (BIS) is the counterpart of x-ray photoemission spectroscopy (XPS). It reveals information on the unoccupied density of states above the Fermi level while XPS provides information on the occupied density of states below the Fermi level.[44] Oh *et al.*[45] studied the electronic structure of $YbAl_2$ using XPS and BIS. The theoretical partial density of states of $4f$ states of Yb in $YbAl_2$ shown in Fig. 5 shows two big peaks, separated by 1.7 eV from the spin-orbit interaction. The theoretical positions of the $4f$ states and the spin-orbit splitting are quite similar to the experimental data.[45]

The theoretical calculations were performed for zero temperature. Therefore in the calculation of the optical conductivity, we treated Yb in $YbAl_2$ as divalent in the ground state. Figures 6 and 8 show the diagonal component of the optical conductivity of pure bulk $LuAl_2$ and $YbAl_2$ obtained using the three-phase model with different thickness of the oxide layer. Identifying which band pairs contribute to the observed peaks and their band characteristics is important for understanding the origin of peaks in the optical conductivity

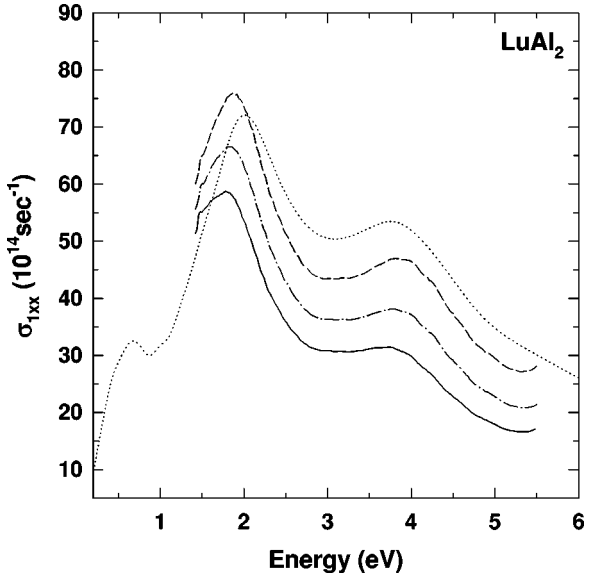

FIG. 6. Diagonal component of the optical conductivity of $LuAl_2$. Dotted line: theoretical data obtained from the TB LMTO using a lifetime broadening proportional to energy. Solid line: experimental data of single crystal of $LuAl_2$. The calculated diagonal component of the optical conductivity of the clean bulk $LuAl_2$ was obtained using the three-phase model with a constant refractive index $n_1=1.7$ and a different thickness of the oxide layer. The dash-dotted line and short-dashed line are the derived optical conductivities of the clean bulk $LuAl_2$ corresponding to 20 Å and 40 Å of the oxide layer, respectively.

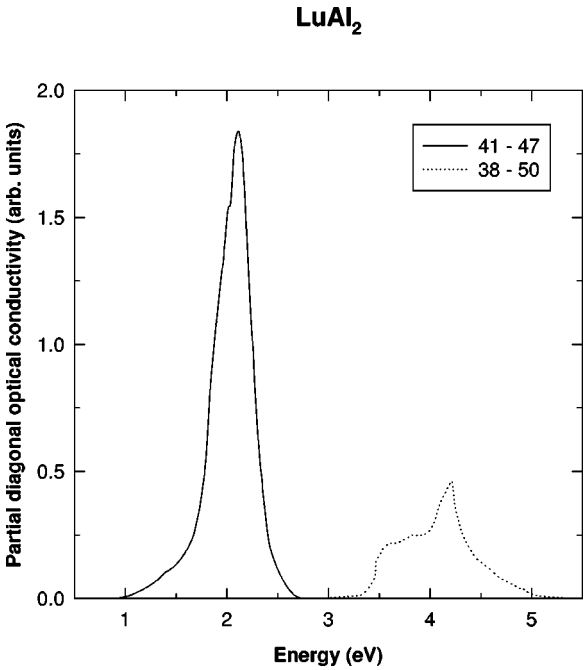

FIG. 7. The contribution of particular interband transitions to the diagonal optical conductivity for peaks at 2.0 eV and 4.0 eV for $LuAl_2$. (In assigning the band numbers in Fig. 2, one should double-count each band due to the degeneracy of states for the paramagnetic $LuAl_2$.)

spectrum. For $LuAl_2$, there are three peaks in the theoretical optical spectrum, one small peak around 0.7 eV, and two big peaks near 2.0 eV and 4.0 eV as shown in Fig. 6. The big peak at 2.0 eV is dominated by the interband transitions between occupied bands (41–46) to unoccupied bands (47–52). The transition pairs are $41\rightarrow47$, $42\rightarrow48$, $43\rightarrow49$, etc. The occupied bands have Al p character hybridized with d bands. The unoccupied bands have Lu d and Al d mixed character. In numbering bands, due to the degeneracy of spin-up and spin-down states for the paramagnetic $LuAl_2$, one should double-count each band. The initial and final band characters participating in the interband transitions should satisfy the selection rule $\Delta l=\pm1$. The transitions around 2.0 eV occur near the line of Γ–L in the irreducible Brillouin zone of the fcc lattice. The peak at 4.0 eV comes from occupied bands (38–46) to unoccupied bands (50–60). The contributions of particular bands to interband transitions in the diagonal optical conductivity for peaks at 2.0 eV and 4.0 eV for $LuAl_2$ are shown in Fig. 7.

In Fig. 6 the solid line is for the experimental data of single crystal of $LuAl_2$. To consider the oxide layer, the three phase model has been used. The optical conductivity of clean $LuAl_2$ is calculated using the measured optical conductivity of the single crystal of $LuAl_2$ with an assumed thickness and refractive index of the oxide layer. Dash-dotted and short-dashed lines are the calculated optical conductivity of clean bulk $LuAl_2$ with the assumption of constant refractive index $n_1=1.7$ and thicknesses of the oxide layer of 20 Å and 40 Å, respectively. As shown in Fig. 6, as the thickness of the oxide layer increases the calculated optical conductivity of the clean bulk sample increases.

In Fig. 8, the theoretical optical conductivity of $YbAl_2$ obtained using the TB-LMTO within the LDA using a lifetime broadening proportional to energy is represented by the dotted line. In the calculation, the $4f$ electrons of Yb are also treated as valence electrons like those of Lu. For $YbAl_2$, the situation is similar to that for $LuAl_2$, except for a big peak at lower energy in the theoretical spectrum. This peak at 0.5 eV arises mainly from the $4f$ states in Yb in $YbAl_2$ because the $4f$ states of Yb are close to the Fermi level. Interband transitions between bands 43–45, 43–46, 44–45, and 44–46 contribute importantly to the peak at 0.5 eV. Occupied bands 43 and 44 are located close to the Fermi level and mostly of Yb $4f$ character. The unoccupied bands 45 and 46 above the Fermi level are of Yb $5d$ character. Figure 9 shows contributions of particular bands to the interband transitions of $YbAl_2$. The optical conductivity of clean $YbAl_2$ is calculated by using the measured optical conductivity of the single crystal of $YbAl_2$ with an assumed thickness and refractive index of the oxide layer. Dash-dotted and short-dashed lines are the calculated optical conductivities of the clean bulk $YbAl_2$. For the calculation, we assumed a constant refractive index of $n_1=1.7$. The assumed thickness of the oxide layers are 30 Å and 50 Å, respectively. We notice a small flat shoulder around 1.6 eV seen in experiment and around 1.7 eV in theory in the optical conductivity. A wide shoulder between 3.0 and 4.0 eV is shown in both theoretical and experimental spectra as shown in Fig. 8. Ellipsometry is surface sensitive in that the measured optical conductivity is not correct if the surface is oxidized. As already discussed, as the oxide refractive index or thickness increases, the optical conductivity of the clean bulk sample, determined from measurements on the oxidized sample, increases. For $LuAl_2$ as

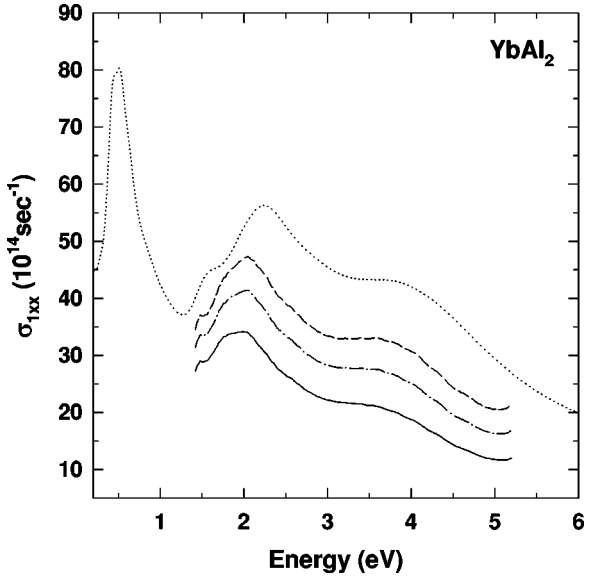

FIG. 8. Diagonal component of the optical conductivity of $YbAl_2$. Dotted line: calculated from the TB LMTO using a lifetime broadening proportional to energy. Solid line: experimental data. The calculated diagonal component of the optical conductivity of the clean bulk $YbAl_2$ was obtained using the three-phase model with a constant refractive index $n_1 = 1.7$ and different thickness of the oxide layer. Dash-dotted line and short-dashed line are the derived optical conductivities of the clean bulk $YbAl_2$ corresponding to 30 Å and 50 Å of the oxide layer, respectively.

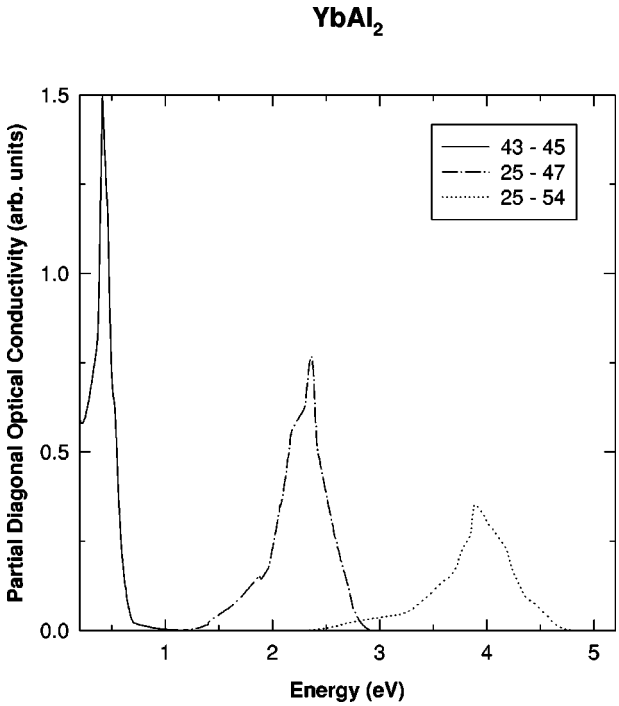

FIG. 9. The contribution of particular interband transitions to the diagonal optical conductivity for peaks at 0.5 eV, 2.0 eV, and 4.0 eV for $YbAl_2$. (In assigning the band numbers in Fig. 3, one should double-count each band due to the degeneracy of states for the paramagnetic $YbAl_2$.)

the oxide thickness increases, the feature around 4.0 eV becomes more prominent. It agrees well with the theoretical calculation around 4.0 eV.

VIII. SUMMARY AND CONCLUSION

The optical conductivities of single crystals of $LuAl_2$ and $YbAl_2$ have been measured between 1.4 and 5.5 eV for $LuAl_2$ and between 1.4 and 5.2 eV for $YbAl_2$. The experimental optical conductivity spectra of single crystals of $LuAl_2$ and $YbAl_2$ agree well with the calculated values obtained from the self-consistent TB-LMTO method based on the LDA formalism except for a difference in magnitude, partially from the effect of the oxide overlayer. Correcting the data with a three-phase model, we find the oxide overlayer reduces the magnitude of the optical conductivity and smoothes out some features. The difference between the electronic structure of $LuAl_2$ and $YbAl_2$ is that the $4f$ states of $YbAl_2$ are located near the Fermi energy level while those of $LuAl_2$ are located well below the Fermi level. The $4f$ electrons near the Fermi level contribute the large peak at 0.5 eV in the theoretical optical conductivity of $YbAl_2$. Experiments have not yet been extended to this energy range to look for the predicted peak in the optical conductivity of $YbAl_2$. Therefore it would be useful to examine it by IR ellipsometry or IR reflectivity measurements.

ACKNOWLEDGMENTS

Ames Laboratory is operated for the U.S. Department of Energy by Iowa State University under Contract No. W-7405-Eng-82. This work was supported by the Director for Energy Research, Office of Basic Energy Science.

*Permanent address: Department of Physics, Kongju National University, Kongju, Chungnam 314-701, Korea.

[1] Y. B. Barash and J. Barak, J. Phys. F: Met. Phys. **14**, 1531 (1984).
[2] J. S. Abell, J. X. Boucherle, R. Osborn, B. D. Rainford, and J. Schweizer, J. Magn. Magn. Mater. **31**, 247 (1983).
[3] E. W. Lee and J. F. D. Montenegro, J. Magn. Magn. Mater. **22**, 282 (1981).
[4] G. Chelkowska, J. Magn. Magn. Mater. **127**, L37 (1993).
[5] B. Vlcek, E. Seidi, and H. W. Weber, Jpn. J. Appl. Phys., Part 1 **26**, 967 (1987).
[6] J. R. Cooper, Solid State Commun. **9**, 1429 (1971).
[7] J. Reichelt and K. Winzer, Phys. Status Solidi B **89**, 489 (1978).
[8] C. A. Luengo and M. B. Maple, Solid State Commun. **12**, 757 (1973).
[9] R. Stiller, H. Merz, W. Drewes, and H.-G. Purwins, J. Phys. (Paris), Colloq. **C9**, 997 (1987).
[10] A. C. Switendick, in *Proceedings of the 10th Rare Earth Research Conference*, Carefree, Arizona, 1973, edited by C. J. Kevane and T. Mueller (U.S. Atomic Energy Commission, Oak Ridge, TN, 1973), Vol. 1, p. 235.
[11] A. Hasegawa and A. Yanase, J. Magn. Magn. Mater. **15**, 887 (1980).
[12] M. Magnitskaya, G. Chelkowska, G. Borstel, M. Neumann, and H. Ufer, Phys. Rev. B **49**, 1113 (1994).
[13] Yu. P. Smirnov, A. E. Sovestnov, G. I. Terekhov, A. V. Tyunis,

and V. A. Shaburov, Fiz. Tverd. Tela (Leningrad) **30**, 3513 (1988) [Sov. Phys. Solid State **30**, 2021 (1988)].
[14] T. Jarlborg, A. J. Freeman, and D. D. Koelling, J. Appl. Phys. **53**, 2140 (1982).
[15] W. E. Pickett and B. M. Klein, J. Less-Common Met. **93**, 219 (1983).
[16] T. Jarlborg, A. J. Freeman, and D. D. Koelling, J. Magn. Magn. Mater. **60**, 291 (1986).
[17] K. J. Kim and D. W. Lynch, J. Phys.: Condens. Matter **5**, 5971 (1993).
[18] B. I. Min, H. J. F. Jansen, T. Oguchi, and A. J. Freeman, J. Magn. Magn. Mater. **59**, 277 (1986).
[19] S. B. M. Hagström, P. O. Heden, and H. Löfgren, Solid State Commun. **8**, 1245 (1970).
[20] B. I. Min, H. J. F. Jansen, T. Oguchi, and A. J. Freeman, J. Magn. Magn. Mater. **61**, 139 (1986).
[21] S. E. Haszko, Trans. Metall. Soc. AIME **221**, 201 (1961).
[22] A. Palenzona, J. Less-Common Met. **29**, 289 (1972).
[23] D. E. Aspnes and A. A. Studna, Appl. Opt. **14**, 220 (1975).
[24] J. Y. Rhee, Ph.D. thesis, Iowa State University, 1992.
[25] R. M. A. Azzam and N. M. Bashara, *Ellipsometry and Polarized Light* (North-Holland, Amsterdam, 1977).
[26] E. A. Irene, Thin Solid Films **233**, 96 (1993).
[27] T. D. Burleigh, S. Wagner, and T. F. Ciszek, Sol. Cells **13**, 179 (1984).
[28] P. J. McMarr, K. Vedam, and J. Narayan, J. Appl. Phys. **59**, 694 (1986).
[29] U. Rossow, in *Linear and Nonlinear Optical Spectroscopy of Surfaces and Interfaces*, edited by J. F. McGilp, D. Weaire, and C. H. Patterson (Springer-Verlag, Berlin, 1995), Chap. 3, p. 53.
[30] W. H. Press, B. P. Flannery, S. A. Teukolskey, and W. T. Vetterling, *Numerical Recipes in C* (Cambridge University Press, Cambridge, 1988).
[31] U. von Barth and L. Hedin, J. Phys. C **5**, 1629 (1972).
[32] R. Kubo, J. Phys. Soc. Jpn. **12**, 570 (1957).
[33] K. J. Kim, T. C. Leung, B. N. Harmon, and D. W. Lynch, J. Phys.: Condens. Matter **6**, 5069 (1994).
[34] J. E. Müller, O. Jepsen, and J. W. Wilkins, Solid State Commun. **42**, 365 (1982).
[35] K. A. Gschneidner, Jr., *Specialty Inorganic Chemicals* (The Royal Society of Chemistry, London, 1981).
[36] K. Zukowska, Ph.D. thesis, Technical University of Wroclaw, Wroclaw, 1975.
[37] D. A. G. Bruggemann, Ann. Phys. (Leipzig) **24**, 636 (1935).
[38] T. Marcinow, Ph.D. thesis, Technical University of Wroclaw, Wroclaw, 1975.
[39] K. Zukowska and E. Oleszkiewicz, Thin Solid Films **224**, 217 (1993).
[40] A. K. Burnham and G. T. Jameson, J. Vac. Sci. Technol. A **5**, 1713 (1987).
[41] Katsuhiko Takegahara, Physica B **186-188**, 850 (1993).
[42] A. C. Gossard, V. Jaccarino, and J. H. Wernick, Phys. Rev. **133**, A881 (1964).
[43] R. E. Hungsberg and K. A. Gschneidner, Jr., J. Phys. Chem. Solids **33**, 401 (1972).
[44] F. U. Hillebrecht and M. Campagna, *Handbook on the Physics and Chemistry of Rare Earths*, edited by K. A. Gschneidner, Jr., L. Eyring and S. Hüfner (North-Holland, Ansterdam, 1987), Vol. 10, Chap. 70.
[45] S.-J. Oh, J. W. Allen, M. S. Torikachvili, and M. B. Maple, J. Magn. Magn. Mater. **52**, 183 (1985).